

# Resonant Ta Doping for Enhanced Mobility in Transparent Conducting SnO<sub>2</sub>

Benjamin A. D. Williamson,<sup>#</sup> Thomas J. Featherstone,<sup>#</sup> Sanjayan S. Sathasivam, Jack E. N. Swallow, Huw Shiel, Leanne A. H. Jones, Matthew J. Smiles, Anna Regoutz, Tien-Lin Lee, Xueming Xia, Christopher Blackman, Pardeep K. Thakur, Claire J. Carmalt, Ivan P. Parkin, Tim D. Veal,<sup>\*</sup> and David O. Scanlon<sup>\*</sup>



Cite This: *Chem. Mater.* 2020, 32, 1964–1973



Read Online

ACCESS |



Metrics & More

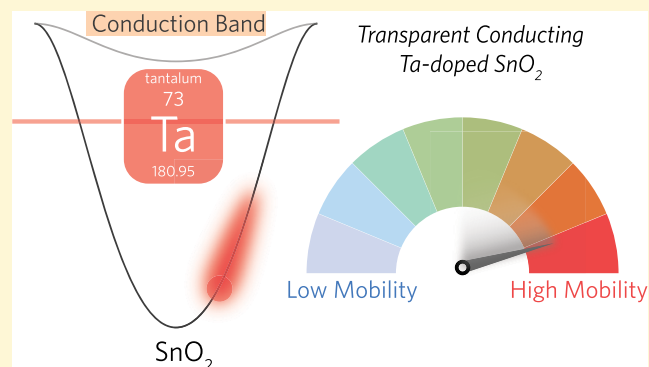


Article Recommendations



Supporting Information

**ABSTRACT:** Transparent conducting oxides (TCOs) are ubiquitous in modern consumer electronics. SnO<sub>2</sub> is an earth abundant, cheaper alternative to In<sub>2</sub>O<sub>3</sub> as a TCO. However, its performance in terms of mobilities and conductivities lags behind that of In<sub>2</sub>O<sub>3</sub>. On the basis of the recent discovery of mobility and conductivity enhancements in In<sub>2</sub>O<sub>3</sub> from resonant dopants, we use a combination of state-of-the-art hybrid density functional theory calculations, high resolution photoelectron spectroscopy, and semiconductor statistics modeling to understand what is the optimal dopant to maximize performance of SnO<sub>2</sub>-based TCOs. We demonstrate that Ta is the optimal dopant for high performance SnO<sub>2</sub>, as it is a resonant dopant which is readily incorporated into SnO<sub>2</sub> with the Ta 5d states sitting  $\sim 1.4$  eV above the conduction band minimum. Experimentally, the band edge electron effective mass of Ta doped SnO<sub>2</sub> was shown to be  $0.23m_0$ , compared to  $0.29m_0$  seen with conventional Sb doping, explaining its ability to yield higher mobilities and conductivities.



## INTRODUCTION

Transparent conducting oxides (TCOs) are materials which possess the generally mutually exclusive properties of high electrical conductivity and optical transparency. These properties are achieved through degenerate doping of wide band gap semiconductors ( $E_g > 3.1$  eV) giving rise to applications in a variety of crucial modern technologies such as touch screen displays, solar cells, low emissivity windows, and gas sensors.<sup>1–6</sup>

Arguably the most successful TCO in terms of both optoelectronic properties and commercial success is In<sub>2</sub>O<sub>3</sub> doped with Sn (ITO), which demonstrates resistivities as low as  $\sim 8 \times 10^{-5} \Omega \text{ cm}$  and carrier concentrations exceeding  $10^{21} \text{ cm}^{-3}$  while retaining >90% visible light transparency.<sup>7,8</sup> ITO dominates the electronics market, however, due to the scarcity and high cost of indium, there is a pressing need to move toward alternative earth abundant TCOs particularly for applications requiring large surface areas such as photovoltaic devices and low emissivity glass coatings.<sup>9</sup>

SnO<sub>2</sub>-based TCOs are often used in such applications due to both their durability as well as the abundance and low cost of Sn. With a suitably wide fundamental band gap of  $\sim 3.6$  eV, undoped SnO<sub>2</sub> has been reported to have resistivities of  $\sim 10^{-2}$  to  $10^{-3} \Omega \text{ cm}$ ,<sup>10</sup> while *n*-type doping has achieved resistivities of  $\sim 10^{-4} \Omega \text{ cm}$ .<sup>4,11</sup> Such doping is achieved by the intentional

substitution of Sn or O by elements with a higher oxidation state than the element they are replacing (V cations for the Sn(IV) site or VII anions for the O(VI) site). Traditional wisdom dictates that the best choice of dopant is the element positioned directly to the right of the host element in the periodic table. This represented a logical choice as they should possess both the correct oxidation state and similar ionic radii, thus minimizing lattice distortion which can lower solubility.<sup>4</sup> Thus, Sb (on the Sn-site) or F (on the O site) have typically been the dopants of choice. Both F-doped SnO<sub>2</sub> (FTO) and Sb-doped SnO<sub>2</sub> (ATO) thin films have displayed resistivities of  $\sim 5 \times 10^{-4} \Omega \text{ cm}$ <sup>4,12</sup> and have been successfully deposited with a wide range of techniques including pulsed laser deposition,<sup>13,14</sup> spray pyrolysis,<sup>15,16</sup> sol-gel,<sup>17,18</sup> and sputtering.<sup>19</sup>

Recent reports show that FTO and ATO are inherently self-limiting as mobilities fail to surpass  $\sim 35 \text{ cm}^2 \text{ V}^{-1} \text{ s}^{-1}$  for carrier concentrations  $> 3 \times 10^{20} \text{ cm}^{-3}$ .<sup>20,21</sup> The mechanism for this

Received: November 22, 2019

Revised: February 17, 2020

Published: February 18, 2020



self-limitation was recently shown to be due to the formation of negatively charged fluorine interstitials; as the Fermi energy rises (due to doping) to  $\sim 0.5$  eV above the conduction band minimum (CBM), it becomes more energetically favorable for fluorine to incorporate interstitially, thus acting as an acceptor rather than as a donor, as is the case when incorporated substitutionally.<sup>20</sup> ATO also undergoes self-compensation, arising due to the multivalency of Sb (Sb(III) and Sb(V)), which have both been observed using both Mössbauer spectroscopy<sup>22,23</sup> and XPS studies. Recent DFT studies have proposed two ways in which self-compensation may occur in ATO. First, substitutional Sb defects can only act as a donor when in the V oxidation state and as an acceptor when in the III oxidation state.<sup>24,25</sup> The second limitation, which was originally proposed from an X-ray absorption fine structure (EXAFS) analysis<sup>26,27</sup> and confirmed through density functional theory calculations, was that the clustering of a substitutional Sb ( $\text{Sb}_{\text{Sn}}$ ) adjacent to an oxygen vacancy ( $\text{V}_{\text{O}}$ ) leads to the formation of Sb(III) and a trapped electron in the oxygen vacancy, similar to an F-center.<sup>11</sup>

Recently, however, we have proposed and demonstrated a new doping mechanism for  $\text{In}_2\text{O}_3$  which yields mobilities and conductivities superior to those reported for ITO. We have demonstrated that Mo-doped  $\text{In}_2\text{O}_3$  (IMO) outperforms ITO as Mo behaves very differently from Sn in  $\text{In}_2\text{O}_3$ .<sup>28,29</sup> In ITO, Sn is in the (IV) oxidation state,<sup>30</sup> and the Sn 5s orbitals mix with the In 5s states at the bottom of the conduction band of  $\text{In}_2\text{O}_3$ . As the concentration of Sn is increased, the mixing at the CBM increases, increasing the effective mass of the CBM and lowering the overall mobility of the system. Mo in the IV oxidation state, on the other hand, possesses localized donor d-orbitals that sit resonant in the conduction band, well separated from the CBM. This and reduced mixing of orbitals due to the lack of overlap between the host s states in the CBM and the dopant d states due to their different shapes ensure that minimal hybridization takes place between the dopant states and the CBM. Increasing the concentration of Mo therefore has no adverse effect on the effective mass of the CBM, allowing higher mobilities and conductivities.<sup>29</sup> Other transition metals which have donor d states and incorporate in the IV oxidation state in  $\text{In}_2\text{O}_3$  are Ti,<sup>31</sup> Zr,<sup>32</sup> Hf,<sup>33</sup> and W.<sup>34</sup> Doping  $\text{In}_2\text{O}_3$  with these have all demonstrated higher mobilities than ITO, indicating similar behavior to Mo.

For  $\text{SnO}_2$ , the ideal donor dopant should therefore be of a similar ionic radius to either Sn or O, possess donor states that sit high in the conduction band, and not hybridize with the host Sn 5s states, while being in the correct oxidation state. On the basis of the successful dopants in  $\text{In}_2\text{O}_3$ , likely candidates would be transition metals which are stable in a V oxidation state. Three such elements exist, V, Nb, and Ta. Previous experimental studies have shown V to not be a shallow donor in  $\text{SnO}_2$  with V 3d states sitting 1.1 eV above the valence band maximum (VBM).<sup>35</sup> As such, V can be ruled out as a dopant. Nb doping of  $\text{SnO}_2$  has demonstrated moderate results experimentally, with high mobilities for  $\text{SnO}_2$  but suffering from low carrier concentrations, in most cases failing to reach  $1 \times 10^{20} \text{ cm}^{-3}$ .<sup>36–38</sup> Therefore, Nb doping warrants further investigation here from a theoretical perspective. The last of the three V oxidation state candidate dopants, Ta, has shown significant promise experimentally. Thin films of Ta-doped  $\text{SnO}_2$  (TaTO) have displayed resistivities as low as  $1.8 \times 10^{-4} \Omega \text{ cm}$  and have been fabricated by a wide array of deposition methods.<sup>39–50</sup> TaTO also displays exceedingly high

mobilities of up to  $83 \text{ cm}^2 \text{ V}^{-1} \text{ s}^{-1}$  when deposited by pulsed laser deposition,<sup>39</sup> in particular, and up to  $49 \text{ cm}^2 \text{ V}^{-1} \text{ s}^{-1}$  when deposited by sputtering<sup>50</sup> (at carrier concentrations of  $2.7 \times 10^{20} \text{ cm}^{-3}$  and  $2.2 \times 10^{20} \text{ cm}^{-3}$ , respectively). This surpasses the upper mobility limits displayed by both ATO and FTO. Indeed, in cases where TaTO does not surpass the upper reported mobilities, comparative studies show that TaTO deposited by the same method as ATO displayed higher mobilities<sup>48</sup> for the same carrier concentrations. Crucially, the origin of this improvement in performance of TaTO films over other doped  $\text{SnO}_2$  alternatives has never been elucidated.

In this study, we use hybrid density functional theory to examine the suitability of Nb and Ta as an alternative dopant for  $\text{SnO}_2$  and compare it to conventional Sb and F dopants. A consistent picture emerges of Ta as the ideal dopant for  $\text{SnO}_2$ , possessing resonant donor states high above the CBM and minimal hybridization with CBM states. We probe the electronic structure differences between Ta and Sb dopants using semiconductor statistics modeling and hard X-ray photoelectron spectroscopy (HAXPES) of aerosol assisted chemical vapor deposition (AACVD) grown TaTO and ATO thin films. Crucially, our experimental characterization supports our computational analysis, indicating that Ta is the optimum dopant for high performance  $\text{SnO}_2$ .

## METHODS

**Computational Methodology.** *Ab initio* density functional theory (DFT) calculations were carried out on  $\text{SnO}_2$  using a plane-wave basis within the periodic code, VASP.<sup>51–54</sup> The projector-augmented wave method (PAW)<sup>55,56</sup> was used to describe the interaction between the core electrons (Sn[Kr], O[He], and Ta[Xe]) and the valence electrons. The hybrid functional used was PBE0 developed by Adamo and Barone,<sup>57,58</sup> which partially addresses the self-interaction error present in local functionals thus allowing for a better description of the band gap and electronic properties of  $\text{SnO}_2$ . PBE0 incorporates 25% of exact Fock exchange to the PBE (Perdew–Burke–Ernzerhoff)<sup>59</sup> formalism. For Sn-based TCOs in particular, PBE0 has been shown to yield electronic structure in excellent agreement with experimental results.<sup>11,20,60,60–69</sup>

A full description of all calculations performed is provided in the Supporting Information (SI section 1) and includes the calculation of the formation energies of each defect and its charge state through the methods described by Neugebauer and Van de Walle.<sup>70</sup> The relative dopant concentrations used in the cells correspond to  $\sim 4\%$  for Ta and Sb and  $\sim 2\%$  for F, respectively. To account for the finite size effects of the defect supercells, both an image-charge correction and band filling correction were used. The image-charge correction used herein was formulated by Lany and Zunger<sup>71</sup> and adapted for noncubic systems by Hine et al.<sup>72</sup> This correction accounts for the interaction of a charged defect with its periodic images. The latter correction remedies the unphysical band filling present in finite-sized supercells in order to regain the dilute limit and is implemented in the scheme by Lany and Zunger.<sup>71</sup> Simulation of the experimental conditions under which the samples were deposited (800 K, 1 atm) was performed using a formalism developed by Reuter and Scheffler<sup>73</sup> (SI eq 6), which has been used to successfully simulate F-doped  $\text{SnO}_2$  films deposited by atmospheric pressure chemical vapor deposition (APCVD) in our previous work.<sup>20</sup> Due to the folded nature of the energy bands present in large supercells, the band unfolding code “BandUP” by Medeiros et al.<sup>74,75</sup> was utilized to obtain a primitive cell representation of the band structure of the doped supercells.

**Thin Film Fabrication.** Thin films of  $\text{SnO}_2$ :Ta and  $\text{SnO}_2$ :Sb were deposited by aerosol assisted chemical vapor deposition (AACVD). All precursors were purchased from Sigma-Aldrich and used as received. AACVD depositions were carried out on a custom built cold-wall reactor where the substrate ( $\sim 50 \text{ nm SiO}_2$  barrier-coated float glass) was positioned on a graphite block containing a Watmann

cartridge heater regulated by a Pt–Rh cartridge heater. A stainless steel top plate was positioned 0.8 cm above the substrate to promote laminar flow. The tantalum doped SnO<sub>2</sub> films were grown using a dual pot AACVD process using butyltin trichloride (0.3 mL, 1.77 mmol) dissolved in dry methanol (10 mL, 394 mmol) and tantalum(V) ethoxide (5, 10, 15, 20 mol %) dissolved in dry toluene (10 mL, 124.7 mmol). The two solutions were atomized using a Johnson Matthey Liquifog piezoelectric ultrasonic humidifier with the tin precursor flow rate kept at 0.6 L min<sup>-1</sup> using air (BOC, 99.99%), and the tantalum precursor flow rate was kept at 0.6 L min<sup>-1</sup> using nitrogen (BOC, 99.99%). The two flows were then mixed at a Y junction and delivered to the CVD reactor. The glass substrate was maintained at 500 °C. The antimony doped SnO<sub>2</sub> films were grown similar to our previously reported method<sup>11</sup> on glass substrates at 450 °C using a one-pot AACVD process where the butyltin trichloride (0.2 mL, 1.06 mmol) and antimony(III) ethoxide (2, 6, 9, 11, 15 mol %) were dissolved in methanol (10 mL, 394 mmol). The carrier gas was air, and the flow rate was 1 L min<sup>-1</sup>. At the end of the depositions for both systems, the reactor was turned off and cooled under a flow of nitrogen until 100 °C, after which point the samples were removed. The coated substrates were handled and stored in air.

**Thin Film Characterization.** Hall effect measurements were carried out in the van der Pauw geometry to determine the sheet resistance, free carrier concentration, and mobility. A square array of Ohmic contacts was arranged on 1 cm<sup>2</sup> samples that were subjected to an input current of 1 mA and a calibrated magnetic field of 0.58 T.

Transmission spectra were obtained using a Shimadzu UV–vis–IR 3700 spectrophotometer with an integrating sphere detector and were measured over a range of  $\lambda = 250\text{--}2500$  nm to cover the visible and near-infrared regions.

Infrared (IR) reflectance measurements were performed using a Bruker Vertex 70v Fourier-transform infrared (FTIR) spectrometer. A CaF<sub>2</sub> beam splitter and DLaTGS detector were used, and spectra were recorded over an energy range of 0.25–1.25 eV, so the plasma resonance cutoff could be observed for all samples.

Hard X-ray photoemission spectroscopy (HAXPES) was performed at the 109 beamline at the Diamond Light Source (Didcot, UK). A photon energy of 5.95 keV was selected using a Si(111) double-crystal monochromator and a Si(004) channel-cut crystal as a post monochromator. The beam size at the sample was  $40 \times 20 \mu\text{m}^2$  with a grazing incident angle of 87.5° with respect to the surface normal. Photoelectrons were detected using an EW4000 photoelectron analyzer from VG Scienta (Uppsala, Sweden). Calibration of the binding energy scale was performed using the Fermi edge and the 4f core level lines of a gold reference sample. The gold Fermi edge was fitted to obtain an experimental resolution of ~200 meV.

X-ray diffraction (XRD) measurements were collected on a modified Bruker-AXS D8 diffractometer with parallel beam optics fitted with a PSD LynxEye silicon strip detector to collect diffracted X-ray photons. X-rays were generated using a Cu source with Cu K $\alpha_1$  and Cu K $\alpha_2$  radiation of wavelengths 1.54056 and 1.54439 Å, respectively, at an intensity ratio of 2:1 and at 40 kV and 30 mA. The incident beam angle was kept at 1°, and the angular range of the patterns collected was  $10^\circ < 2\theta < 65^\circ$  with a step size of 0.05° counted at 0.5 s per step.

## RESULTS AND DISCUSSION

**Defect Thermodynamics and Band Structure.** Defect thermodynamics and band structures have been calculated for Nb and Ta doped SnO<sub>2</sub>. As described in detail in the SI, Nb is found to be neither a shallow nor a resonant donor. Therefore, the remainder of this work focuses on Ta doping.

To understand why Ta has the potential to surpass Sb and F as a dopant in SnO<sub>2</sub>, the thermodynamic transition levels of the Ta-related species were calculated and are presented in Figure 1, showing the formation energy of a defect and its respective charge states as a function of Fermi energy. Also shown are the Sb and F defect species together with the

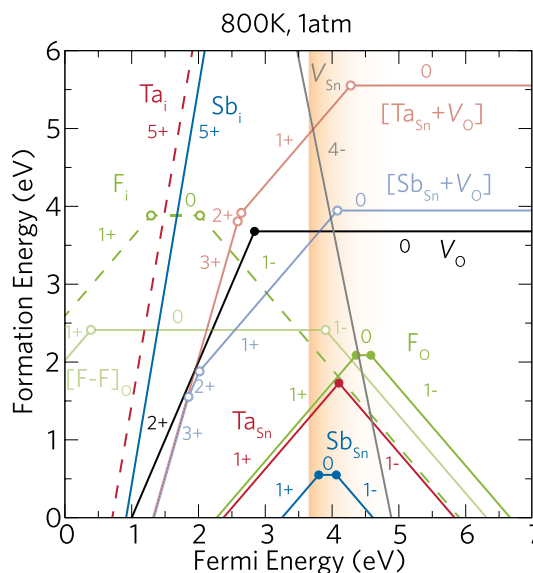


**Figure 1.** Calculated formation energies for the TaTO (red), ATO (gray), and FTO (green) related defects as a function of Fermi energy under experimental synthesis conditions (800 K and 1 atm). The VBM is set at 0 eV, and the conduction band is depicted by the graded orange area. A full discussion of the Sb and F related defects can be found in refs 11 and 20, respectively.

dominant intrinsic defect species ( $V_{\text{Sn}}$  and  $V_{\text{O}}$ ) as reported previously in refs 11 and 20. The transition levels shown are presented under 800 K/1 atm conditions in order to represent the growth conditions of the AACVD grown films in this work.

The substitutional impurity  $\text{Ta}_{\text{Sn}}$  is found to be the dominant tantalum species in SnO<sub>2</sub> and acts as a resonant one-electron donor transitioning from the +1 charge state to the –1 charge state at around ~0.5 eV above the CBM. These results are in line with the high conductivities seen in the experiment both here and elsewhere.<sup>39–49</sup>

The ability to push the Fermi level high into the conduction band is critical for maximizing the charge carrier concentrations and thus conductivities. In Sb-doped SnO<sub>2</sub>, despite  $\text{Sb}_{\text{Sn}}$  acting as a resonant donor, the +1 charge state transitions to the neutral charge state at ~0.15 eV above the CBM. In F-doped SnO<sub>2</sub>, the Fermi level also reaches ~0.5 eV above the CBM before self-compensation from fluorine interstitial defects occurs, thus making Ta competitive as a replacement.<sup>20</sup> Reaching this Fermi level is also dependent on the solubility of Ta in SnO<sub>2</sub>. At the CBM, it can be seen that although  $\text{Ta}_{\text{Sn}}$  (~1.27 eV) possesses a higher formation energy than  $\text{Sb}_{\text{Sn}}$  (~0.40 eV) at the CBM, it is still lower than  $\text{F}_{\text{O}}$  (~1.33 eV). As this level is reachable in FTO thin films, it is highly likely that TaTO thin films will also reach high carrier concentrations. Indeed, it can be expected that under nonequilibrium conditions such as CVD, the solubility will be enhanced due to the inclusion of kinetic effects.<sup>76</sup>

As previously stated, both F-doped SnO<sub>2</sub> and Sb-doped SnO<sub>2</sub> undergo defect compensation mechanisms that can severely limit the electron mobility and thus the conductivity of tin dioxide.<sup>11,20</sup> From our calculations, it is shown that the only limiting factor to Ta as a dopant is the transition to the –1 charge state, whereby Ta(V) accepts two electrons to become Ta(III) and thus acts as an acceptor. Additionally, the formation of  $\text{Ta}_i$  is prohibitively high (~13.54 eV in the neutral charge state) under 800 K/1 atm growth conditions and acts as

a donor and thus is not expected to form or act as a mechanism for self-compensation.

Similarly, it was found that the clustering of  $\text{Ta}_{\text{Sn}}$  and  $\text{V}_{\text{O}}$  was highly unfavorable ( $\sim 13.54$  eV in the neutral charge state), and they preferred to dissociate from each other with the associated formation energy being  $\sim 0.38$  eV higher for the neutral charge state. Unlike in ATO, therefore, it is highly unlikely that these clusters will exist.

The high mobilities reported in TaTO thin films are indicative of the lack of dopant hybridization at the CBM as seen in Mo-doped  $\text{In}_2\text{O}_3$  (IMO),<sup>28,29</sup> resulting in no increase in effective mass with increased carrier concentration. The effect of Ta on the band structure of  $\text{SnO}_2$  is shown in Figure 2, which displays the unfolded supercell band structures of

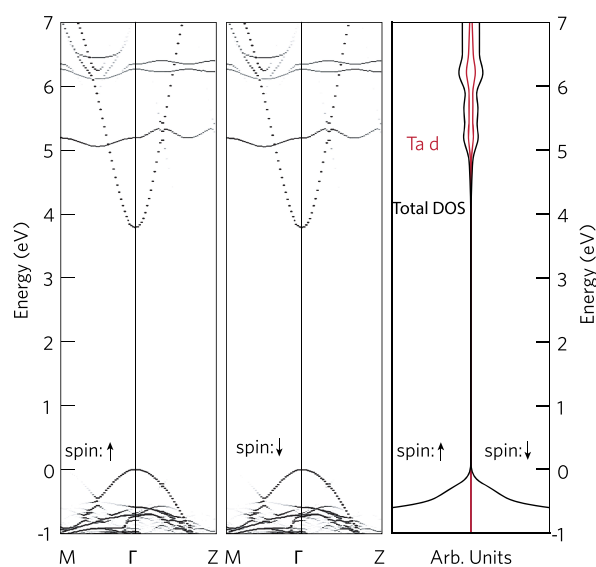


**Figure 2.** Unfolded band structure and DOS for the ionized (+1 charge state) substitutional  $\text{Ta}_{\text{Sn}}$  defect. The band structure is decomposed into both spin-up and spin-down channels, and the VBM is set to 0 eV.

substitutional Ta ( $\text{Ta}_{\text{Sn}}$ ) in the +1 (ionized) charge state in both the spin-up and spin-down configurations. Also shown is the density of states (DOS) pertaining to the Ta states. Unfolded band structures are given for  $\text{Sb}_{\text{Sn}}$  and  $\text{F}_{\text{O}}$  for comparison and are found in SI Figures S3 and S4, respectively.

In both spin-up and spin-down configurations, there is no hybridization of the Ta states with the CBM, which is dominated by Sn  $s$  and O  $2s$  states, which gives rise to its highly dispersive character and low effective mass of  $\sim 0.26m_e$  typical of n-type metal oxides.<sup>4,11,61,77</sup> In TaTO, it can be seen that the Ta  $5d$  states occur  $\sim 1.40$  eV above the CBM in both spin configurations with further Ta  $5d$  “bands” appearing  $\sim 2.47$  eV above the CBM. These bands have 70% Ta  $d$  character mixed with Sn  $s$  and O  $s$  states. For TaTO, the CBM has <1% Ta  $d$  character, indicating minimal perturbation of the CBM states by Ta doping. Conversely, in the band structures for  $\text{Sb}_{\text{Sn}}^{1+}$  and  $\text{F}_{\text{O}}^{1+}$  (SI Figures S3 and S4, respectively), there is around 3% Sb and F character at the CBM. This is shown pictorially in Figure 3a–c by the partial charge densities of each system (TaTO, ATO, and FTO, respectively) at the CBM. The lack of charge density observed around the  $\text{Ta}_{\text{Sn}}$  site (red) indicates there are no Ta states at the CBM. Meanwhile, charge density can be seen around the  $\text{Sb}_{\text{Sn}}$  (blue) and  $\text{F}_{\text{O}}$  sites, indicating that Sb and F contribute states at the CBM. It is clear that for both ATO and FTO, there is significant mixing of the dopant states with those of the host. It is expected, therefore, that no perturbation of the host effective mass will be observed with Ta doping, which gives rise to the high mobilities seen.

## EXPERIMENTAL RESULTS

To experimentally confirm the resonant behavior of Ta in  $\text{SnO}_2$  as predicted by the calculations, Ta and Sb doped  $\text{SnO}_2$  films were deposited by AACVD. The thin films displayed a wide range of electrical properties as shown in Figure 4 and in Table 1. The samples are labeled by the percentage of Ta or Sb in the precursor solution. For the Sb doped films, the highest mobility is  $17.7 \text{ cm}^2 \text{ V}^{-1} \text{ s}^{-1}$  at a carrier concentration of  $3.44 \times 10^{20} \text{ cm}^{-3}$ , corresponding to the lowest resistivity of  $10.3 \times 10^{-4} \Omega \text{ cm}$ . In the Ta doped films, the highest mobility observed was  $25.9 \text{ cm}^2 \text{ V}^{-1} \text{ s}^{-1}$  at a carrier concentration of  $2.65 \times 10^{20} \text{ cm}^{-3}$ , corresponding to a resistivity of  $9.1 \times 10^{-4} \Omega \text{ cm}$ . Films with a higher carrier density of up to  $3.70 \times 10^{20} \text{ cm}^{-3}$  and slightly lower mobility gave resistivities down to  $7.4 \times 10^{-4} \Omega \text{ cm}$ . Literature values for TaTO and ATO are also shown in Figure 4. The literature shows a trend of TaTO achieving higher mobilities than ATO at comparable carrier concentrations, similar to the samples studied in this work. Some exceptions to this are the TaTO samples deposited onto a seed layer to promote preferred orientation and increased crystallinity, which display significantly higher mobilities than

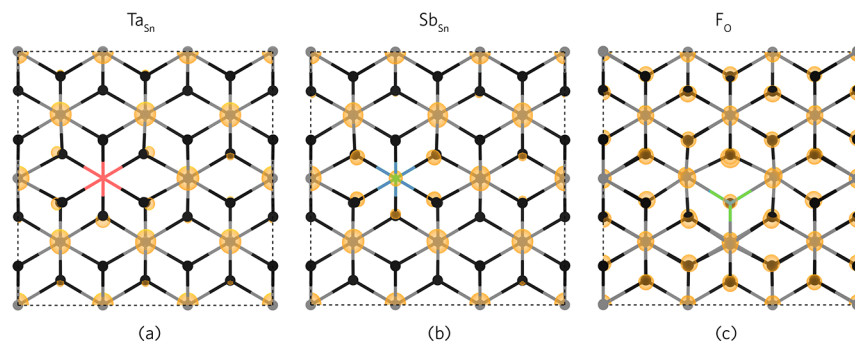


**Figure 3.** Partial charge densities at the CBM of  $\text{SnO}_2$  for  $\text{Ta}_{\text{Sn}}$  (a),  $\text{Sb}_{\text{Sn}}$  (b), and  $\text{F}_{\text{O}}$  (c). The densities highlight the fact that Sb and F both hybridize with the CBM, thus providing a detrimental effect to the band curvature with increased doping concentrations and that Ta does not undergo this same effect.

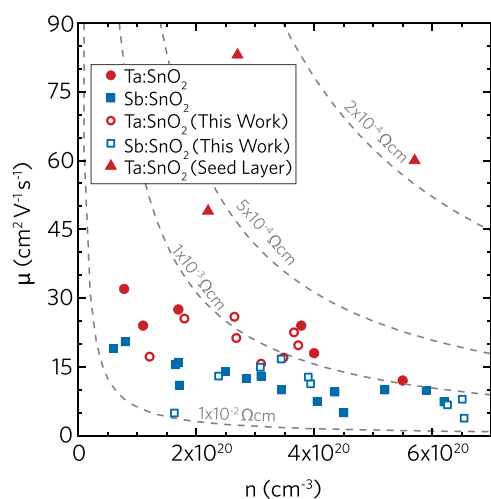


**Figure 4.** Mobility for samples with a range carrier concentrations deposited by AACVD (This work) and Hall properties of ATO and TaTO samples reported throughout the literature.<sup>19,48,78–80</sup> Dashed lines display lines of constant resistivity. Triangular points are TaTO films deposited on seed layers as reported in the literature<sup>39,50</sup>

**Table 1.** Electrical Properties of the “Undoped,” Ta-doped and Sb-doped SnO<sub>2</sub> Films Used in This Work As Determined by Room Temperature Hall Effect Measurements<sup>a</sup>

sample	sheet resistance (Ω/□)	$\rho$ (Ωcm)	$\mu$ (cm <sup>2</sup> V <sup>-1</sup> s <sup>-1</sup> )	$n$ (cm <sup>-3</sup> )
“undoped” SnO <sub>2</sub>	35	$2.97 \times 10^{-3}$	17.2	$1.21 \times 10^{20}$
Ta:SnO <sub>2</sub> (5%)	14	$1.09 \times 10^{-3}$	21.3	$2.68 \times 10^{20}$
Ta:SnO <sub>2</sub> (10%)	8	$7.42 \times 10^{-4}$	22.5	$3.66 \times 10^{20}$
Ta:SnO <sub>2</sub> (15%)	8	$9.08 \times 10^{-4}$	25.9	$2.65 \times 10^{20}$
Ta:SnO <sub>2</sub> (20%)	11	$8.65 \times 10^{-4}$	19.7	$3.73 \times 10^{20}$
Ta:SnO <sub>2</sub> (40%)	13	$1.29 \times 10^{-3}$	15.7	$3.10 \times 10^{20}$
Sb:SnO <sub>2</sub> (2%)	11	$1.03 \times 10^{-3}$	17.7	$3.44 \times 10^{20}$
Sb:SnO <sub>2</sub> (6%)	23	$1.40 \times 10^{-3}$	11.3	$3.94 \times 10^{20}$
Sb:SnO <sub>2</sub> (9%)	33.5	$1.49 \times 10^{-3}$	13.0	$2.38 \times 10^{20}$
Sb:SnO <sub>2</sub> (11%)	128	$7.72 \times 10^{-3}$	5.0	$1.63 \times 10^{20}$
Sb:SnO <sub>2</sub> (15%)	23	$1.49 \times 10^{-3}$	6.7	$6.26 \times 10^{20}$

<sup>a</sup>Percentages given are the Ta or Sb concentration in the precursor solution.

seen elsewhere and highlight the potential of Ta as a dopant.<sup>39,50</sup>

X-ray diffraction patterns are displayed in Figure S5 and are discussed in the text of the Supporting Information.

Experimentally, the difference in the conduction band dispersion expected due to differences in hybridization with the Sn 5s states can be observed as changes in band filling as a function of carrier density. This can also be seen as a difference in the electron effective mass, as the carrier effective mass and band dispersion are related.

Transmission spectra for examples of TaTO and ATO of comparable carrier concentrations,  $3.66 \times 10^{20}$  and  $3.44 \times 10^{20}$  cm<sup>-3</sup>, respectively, are shown in Figure 5a. The transmission at high energies is comparable for the two samples. However, at lower energies, TaTO displays superior transmission. For photovoltaic application, depending on the absorber used, transparency in the near-infrared at energies as low as 1.1 eV can be important. Currently, one of the main applications of FTO is as a transparent electrode in thin film solar cells, so it is likely that commercially TaTO would be used in similar applications, so the increased transmission in the near-IR is important. It should be noted that Zr-doped In<sub>2</sub>O<sub>3</sub> thin films with improved IR transparency have been reported to yield an improvement in power conversion efficiency of perovskite solar cells, due to the lack of parasitic losses in the IR region.<sup>81</sup>

The reflectivity spectra in the near IR range for the same samples is shown in Figure 5b. Reflectivity in this range is caused by scattering of light by free carriers, and the onset of reflection is determined by the plasma frequency,  $\omega_p$ . The energy at which this onset occurs is described by

$$\omega_p = \sqrt{\frac{ne^2}{m^* \epsilon_\infty \epsilon_0}} \quad (1)$$

For these samples of similar carrier concentration, the ATO sample has a reflection onset at a lower energy than the TaTO sample. On the basis of eq 1, this must be due to variation in the carrier effective mass. As  $\omega_p$  is proportional to the inverse of the square root of  $m^*$ , a higher plasma frequency is expected for a lower effective mass. This is indicative that carriers in ATO have a higher effective mass than those in TaTO.

When comparing TaTO and ATO films of equal conductivity, the TaTO films with higher mobility,  $\mu$ , will have lower carrier density,  $n$ , as conductivity,  $\sigma$ , is given by  $\sigma = ne\mu$ . This lower  $n$  leads to lower conduction electron plasma frequency and so increased infrared transparency.

Differences in band filling can be observed as changes in the relationship between the Fermi level and carrier concentration in the film. It was not possible to optically measure the gap for the samples in this study as the absorption edge of the glass substrate is at a lower energy than that of the doped SnO<sub>2</sub> films. However, the Fermi level to valence band maximum separation,  $\Phi = E_F - E_V$ , can be observed in the HAXPES spectra, as emission from the conduction band up to the Fermi level can be observed, as shown in Figure 6a and b. The value obtained will be close to the optical band gap,  $E_{opt}$ , but will vary from it slightly as valence band dispersion does not contribute to  $\Phi$ , as illustrated in Figure 6d. A full description of how the  $\Phi$  values were obtained is given in the Supporting Information. HAXPES is used rather than conventional XPS due to the increased relative cross-section of s states compared with p and d states at higher photon energies and the increased intensity obtained from synchrotron radiation. As the conduction band minimum is primarily of Sn 5s character, the relative intensity of the signal from the conduction band is therefore a lot higher in HAXPES. This enables the  $\Phi$  values to be determined more easily, and the results are plotted in Figure 6c.

The carrier concentration,  $n$ , of the films is related to the Fermi energy,  $E_F$ , by

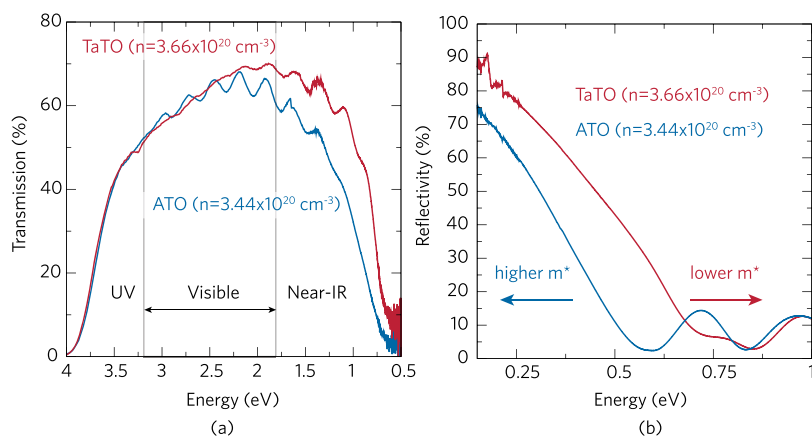


**Figure 5.** (a) The wide range transmission spectra for TaTO and ATO samples with carrier concentrations of  $3.66 \times 10^{20}$  and  $3.44 \times 10^{20} \text{ cm}^{-3}$  respectively. (b) The IR reflectivity spectra for the same two samples showing different onsets for the plasma edge. The expressions for plasma frequency are shown, showing that at constant carrier concentrations the plasma frequency will depend on the inverse of the carrier effective mass.

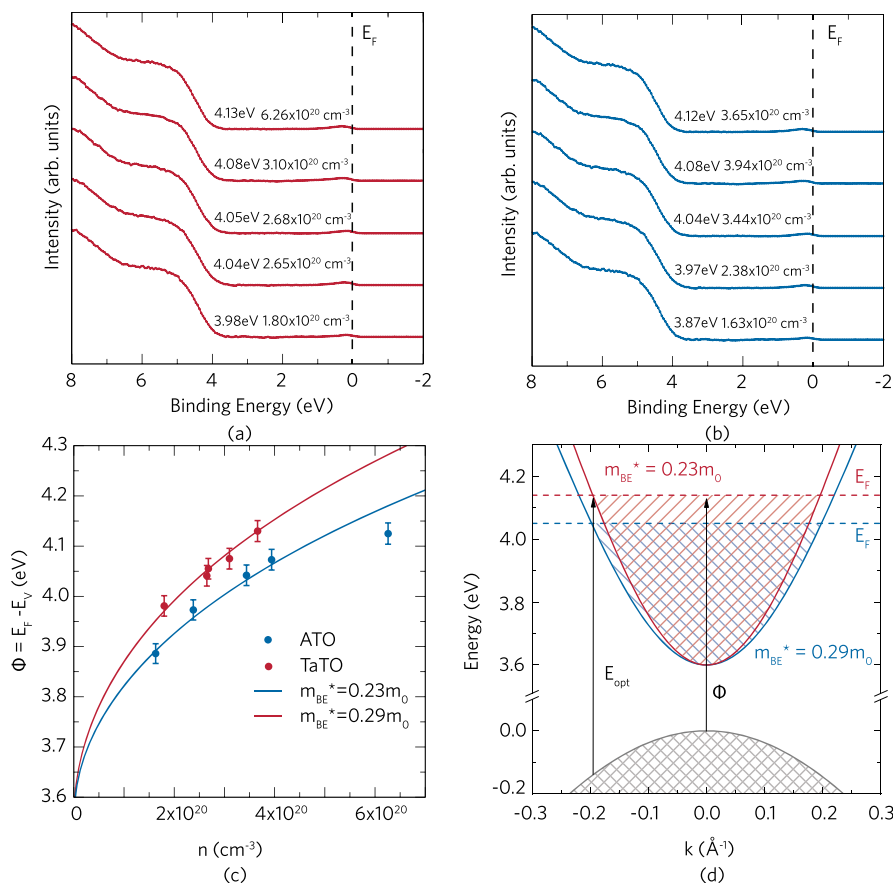


**Figure 6.** The fitted VB edges for HAXPES spectra for a range of carrier concentrations in (a) TaTO and (b) ATO. A Fermi edge has been fitted to the conduction band emission in each spectrum and set to 0 eV. The values presented are  $\Phi$  for each data set. (c) The optical gaps as calculated from valence band and conduction band HAXPES spectra of TaTO and ATO film with a range of carrier concentrations. Fitted lines are calculated using the nonparabolic alpha approximation. (d) The calculated band dispersion for band edge effective masses  $0.23m_0$  (red) and  $0.29m_0$  (blue) demonstrating the difference in band filling by showing the different Fermi levels (dashed lines) for a carrier concentration of  $3.6 \times 10^{20} \text{ cm}^{-3}$ . The optical gap,  $E_{\text{opt}}$  and the Fermi level to VBM separation,  $\Phi$ , are demonstrated for the band edge effective mass of  $0.23m_0$ .

$$n = \int_0^{\infty} D(E) f(E) dE \quad (2)$$

where  $D(E)$  is the energy dependent density of states and  $f(E)$  a Fermi function which is dependent on  $E_F$ .  $D(E)$  is dependent on  $m^*$ ; therefore the relationship between carrier concen-

tration and Fermi level is dependent on the carrier effective mass.

The carrier concentrations of the samples are known from Hall effect measurements and are plotted against  $\Phi$  in Figure 6c. A clear difference between the relationships between  $E_{\text{opt}}$  and  $n$  for the two differently doped materials can be seen with

higher Fermi levels being observed for similar carrier concentrations in TaTO compared to ATO.

$\Phi$  was calculated as a function of  $n$  using eq 2 for a range of band edge effective masses,  $m_{\text{BE}}^*$ , while accounting for conduction band nonparabolicity using the alpha approximation.<sup>82</sup> The calculated lines that fit the data are shown in Figure 6c, and the values of  $m_{\text{BE}}^*$  for TaTO and ATO were found to be  $0.23m_0$  and  $0.29m_0$ , respectively.

Figure 6d shows the calculated band dispersion, using the alpha approximation, where  $E(1 + \alpha E) = \hbar^2 k^2 / 2m_0^*$  and  $\alpha = 1/E_g$ , to account for nonparabolicity, for the effective masses obtained for TaTO and ATO. An increase in band edge effective mass is shown to result in a more dispersed conduction band. The Fermi levels shown are calculated for a carrier concentration of  $3.6 \times 10^{20} \text{ cm}^{-3}$ .

The different CB dispersion should result in discernible differences in HAXPES CB emission as previously shown for a comparison of IMO and ITO.<sup>29</sup> However, the presence of Sn(II) lone pairs introduces intense subgap states, the intensity of which merges into the weak CB emission, as shown in Figure S56 in the SI. This makes detailed comparisons of the conduction band emission as a function of carrier density and dopant type impossible in this case.

The increase in the band edge effective mass and change in dispersion in ATO compared to TaTO is due to hybridization of the Sb 5s with the Sn 5s at the conduction band minimum. Notably, the ATO sample with the highest carrier concentration does not fall on the fitted line for  $m_{\text{BE}}^* = 0.29m_0$  in Figure 6c. This is likely due to higher Sb incorporation causing further hybridization with the CBM, further increasing the band-edge effective mass.

While these values can explain the increase in mobility observed in these Ta doped AACVD films with respect to Sb doping, the differences in effective mass are not enough to explain the high mobilities observed in previous literature. It is of note that the highest mobility samples reported in the literature have all been grown on seed layers promoting a (100) preferred orientation and increased grain size.<sup>39,50</sup> While the mechanism behind these higher mobilities is not fully understood, as, at the high carrier concentrations observed, grain-boundary scattering is expected to have minimal contribution,<sup>83</sup> these samples highlight the potential of TaTO to surpass other SnO<sub>2</sub>-based TCOs. While CVD FTO has benefitted from decades of empirical optimization, it has reached the peak of its self-compensation-limited performance.<sup>20</sup> Meanwhile, CVD of TaTO is in its infancy, but our results and those from other deposition techniques<sup>39,43,50</sup> indicate that the conductivity of CVD TaTO could exceed that of FTO by a factor of 5 or 6 with improved IR transparency.

Bhachu et al. suggested that the mechanism for the improved mobilities seen in IMO compared to ITO was "remote ionized impurity scattering."<sup>28</sup> In the paper, it is suggested that, as the donor state was significantly energetically removed from the CBM, the CBM wave function will be weak close to the donor atom. As a result, the conduction electrons would experience reduced scattering by the donor center's Coulomb potential in comparison to a nonresonant donor. For this mechanism to make a difference in Ta doped SnO<sub>2</sub>, the atomic distance between the Ta donor atoms and the Sn atoms,  $d$ , would need to be comparable or greater than the Thomas–Fermi screening length,  $\lambda_{\text{TF}}$ . The reduction in Coulombic interaction can be expected to be a factor of  $\exp(-d/\lambda_{\text{TF}})$ . The separation of Ta from Sn atoms is about 3.1

Å (ref 84), and the Thomas–Fermi screening length is around 7.0 Å for a carrier concentration of around  $3 \times 10^{20} \text{ cm}^{-3}$ . These values give a factor 0.64 times for Coulomb scattering by donor centers in Ta doped SnO<sub>2</sub> compared to regular donor impurities such as Sb. This corresponds to an increased ionized impurity limited mobility of 1/0.64 or 1.56 times. This difference closely matches the difference in mobility seen in the ATO and TaTO samples studied in this work.

These observations made from the HAXPES data in combination with the results from DFT calculations show clear benefits of the position of the Ta donor states with respect to the CBM. The Ta d states sit resonant in the conduction band, meaning that there is minimal mixing with the host states at the CBM. As a result, the shape of the conduction band is maintained and carrier effective mass is not increased as occurs with traditional dopants, and higher mobilities can be achieved.

## CONCLUSION

Using a combination of hybrid density functional theory calculations, IR reflectivity, and hard X-ray photoelectron spectroscopy, we have demonstrated conclusively that Ta is a resonant donor in SnO<sub>2</sub>. These findings, in combination with previous literature on Ta-doped SnO<sub>2</sub>, indicate that Ta is a superior dopant to both fluorine and antimony, with the capability to yield higher conductivities, higher mobilities, and better IR transparency than either FTO or ATO. These findings suggest that TaTO has the potential to replace FTO as the industrial standard for large surface area applications where a low cost TCO is required.

## ASSOCIATED CONTENT

### Supporting Information

The Supporting Information is available free of charge at <https://pubs.acs.org/doi/10.1021/acs.chemmater.9b04845>.

Computational methodology, Nb-doped SnO<sub>2</sub>, unfolded bandstructures of ATO and FTO, XRD, HAXPEX midgap states, and the full method for experimentally determining Fermi level to VBM separation (PDF)

## AUTHOR INFORMATION

### Corresponding Authors

**Tim D. Veal** – Stephenson Institute for Renewable Energy and Department of Physics, University of Liverpool, Liverpool L69 7ZF, United Kingdom; [orcid.org/0000-0002-0610-5626](https://orcid.org/0000-0002-0610-5626); Email: [T.Veal@liverpool.ac.uk](mailto:T.Veal@liverpool.ac.uk)

**David O. Scanlon** – Department of Chemistry and Thomas Young Centre, University College London, London WC1H 0AJ, United Kingdom; [orcid.org/0000-0001-9174-8601](https://orcid.org/0000-0001-9174-8601); Email: [d.scanlon@ucl.ac.uk](mailto:d.scanlon@ucl.ac.uk)

### Authors

**Benjamin A. D. Williamson** – Department of Chemistry and Thomas Young Centre, University College London, London WC1H 0AJ, United Kingdom; [orcid.org/0000-0002-6242-1121](https://orcid.org/0000-0002-6242-1121)

**Thomas J. Featherstone** – Stephenson Institute for Renewable Energy and Department of Physics, University of Liverpool, Liverpool L69 7ZF, United Kingdom

**Sanjayan S. Sathasivam** – Materials Research Centre, Chemistry Department, University College London, London WC1H 0AJ, United Kingdom; [orcid.org/0000-0002-5206-9558](https://orcid.org/0000-0002-5206-9558)

**Jack E. N. Swallow** – Stephenson Institute for Renewable Energy and Department of Physics, University of Liverpool, Liverpool L69 7ZF, United Kingdom

**Huw Shiel** – Stephenson Institute for Renewable Energy and Department of Physics, University of Liverpool, Liverpool L69 7ZF, United Kingdom

**Leanne A. H. Jones** – Stephenson Institute for Renewable Energy and Department of Physics, University of Liverpool, Liverpool L69 7ZF, United Kingdom

**Matthew J. Smiles** – Stephenson Institute for Renewable Energy and Department of Physics, University of Liverpool, Liverpool L69 7ZF, United Kingdom

**Anna Regoutz** – Department of Chemistry, University College London, London WC1H 0AJ, United Kingdom; [orcid.org/0000-0002-3747-3763](https://orcid.org/0000-0002-3747-3763)

**Tien-Lin Lee** – Diamond Light Source Ltd., Diamond House, Harwell Science and Innovation Campus, Didcot, Oxfordshire OX11 0DE, United Kingdom

**Xueming Xia** – Department of Chemistry, University College London, London WC1H 0AJ, United Kingdom

**Christopher Blackman** – Department of Chemistry, University College London, London WC1H 0AJ, United Kingdom; [orcid.org/0000-0003-0700-5843](https://orcid.org/0000-0003-0700-5843)

**Pardeep K. Thakur** – Diamond Light Source Ltd., Diamond House, Harwell Science and Innovation Campus, Didcot, Oxfordshire OX11 0DE, United Kingdom; [orcid.org/0000-0002-9599-0531](https://orcid.org/0000-0002-9599-0531)

**Claire J. Carmalt** – Materials Research Centre, Chemistry Department, University College London, London WC1H 0AJ, United Kingdom; [orcid.org/0000-0003-1788-6971](https://orcid.org/0000-0003-1788-6971)

**Ivan P. Parkin** – Materials Research Centre, Chemistry Department, University College London, London WC1H 0AJ, United Kingdom

Complete contact information is available at:  
<https://pubs.acs.org/10.1021/acs.chemmater.9b04845>

### Author Contributions

#Contributed equally to this work

### Notes

The authors declare no competing financial interest.

### ACKNOWLEDGMENTS

This work was supported by the Engineering and Physical Sciences Research Council (EPSRC) [grant numbers EP/N01572X/1 and EP/N015800/1]. T.J.F., J.E.N.S., and M.J.S. acknowledge studentship support from the EPSRC Centre for Doctoral Training in New and Sustainable Photovoltaics (Grant No. EP/L01551X/1). H.S. studentship was funded by the EPSRC (Grant No. EP/N509693/1). L.A.H.J.'s studentship was funded by the EPSRC Doctoral Training Partnership (Grant No. EP/R513271/1). The authors thank Diamond Light source for providing beam time and facilities under proposals SI18195-1 and SI21431-1. We are grateful to the UK Materials and Molecular Modelling Hub for computational resources, which is partially funded by EPSRC (EP/P020194/1) and to UCL for the provision of the Legion, Myriad, and Grace supercomputers. Via our membership of the UK's HEC Materials Chemistry Consortium, which is funded by EPSRC (EP/L000202, EP/R029431), this work used the ARCHER UK National Supercomputing Service (<http://www.archer.ac.uk>). D.O.S. and T.D.V. acknowledge membership of the Materials Design Network. NSG Group are acknowledged for

useful discussions and for supplying glass substrates used in this work.

### REFERENCES

- (1) Hosono, H. Recent progress in transparent oxide semiconductors: Materials and device application. *Thin Solid Films* **2007**, *515*, 6000–6014.
- (2) Stadler, A. Transparent Conducting Oxides - An Up-To-Date Overview. *Materials* **2012**, *5*, 661–683.
- (3) Lewis, B. G.; Paine, D. C. Applications and Processing of Transparent Conducting Oxides. *MRS Bull.* **2000**, *25*, 22–27.
- (4) Dixon, S. C.; Scanlon, D. O.; Carmalt, C. J.; Parkin, I. P. N-Type doped transparent conducting binary oxides: an overview. *J. Mater. Chem. C* **2016**, *4*, 6946–6961.
- (5) Parkin, I. P.; Manning, T. D. Intelligent Thermochromic Windows. *J. Chem. Educ.* **2006**, *83*, 393–400.
- (6) Das, S.; Jayaraman, V. SnO<sub>2</sub>: A comprehensive review on structures and gas sensors. *Prog. Mater. Sci.* **2014**, *66*, 112–255.
- (7) Aliyu, M. M.; Hossain, S.; Husna, J.; Dhar, N.; Huda, M. Q.; Sopian, K.; Amin, N. High quality indium tin oxide (ITO) film growth by controlling pressure in RF magnetron sputtering. *2012 38th IEEE Photovoltaic Specialists Conference*; IEEE, 2012; pp 002009–002013.
- (8) Gupta, R.; Ghosh, K.; Mishra, S.; Kahol, P. Structural, optical and electrical characterization of highly conducting Mo-doped In<sub>2</sub>O<sub>3</sub> thin films. *Appl. Surf. Sci.* **2008**, *254*, 4018–4023.
- (9) Minami, T. New n-Type Transparent Conducting Oxides. *MRS Bull.* **2000**, *25*, 38–44.
- (10) Batzill, M.; Diebold, U. The surface and materials science of tin oxide. *Prog. Surf. Sci.* **2005**, *79*, 47–154.
- (11) Ponja, S. D.; Williamson, B. A. D.; Sathasivam, S.; Scanlon, D. O.; Parkin, I. P.; Carmalt, C. J. Enhanced electrical properties of antimony doped tin oxide thin films deposited via aerosol assisted chemical vapour deposition. *J. Mater. Chem. C* **2018**, *6*, 7257–7266.
- (12) Abendroth, T.; Schumm, B.; Alajlan, S. A.; Almogbel, A. M.; Mäder, G.; Härtel, P.; Althues, H.; Kaskel, S. Optical and thermal properties of transparent infrared blocking antimony doped tin oxide thin films. *Thin Solid Films* **2017**, *624*, 152–159.
- (13) Kim, H.; Auyeung, R.; Piqué, A. Transparent conducting F-doped SnO<sub>2</sub> thin films grown by pulsed laser deposition. *Thin Solid Films* **2008**, *516*, 5052–5056.
- (14) Marcel, C.; Hegde, M.; Rougier, A.; Maugy, C.; Guéry, C.; Tarascon, J.-M. Electrochromic properties of antimony tin oxide (ATO) thin films synthesized by pulsed laser deposition. *Electrochim. Acta* **2001**, *46*, 2097–2104.
- (15) Zhi, X.; Zhao, G.; Zhu, T.; Li, Y. The morphological, optical and electrical properties of SnO<sub>2</sub>:F thin films prepared by spray pyrolysis. *Surf. Interface Anal.* **2008**, *40*, 67–70.
- (16) Bisht, H.; Eun, H.-T.; Mehrtens, A.; Aegerter, M. Comparison of spray pyrolyzed FTO, ATO and ITO coatings for flat and bent glass substrates. *Thin Solid Films* **1999**, *351*, 109–114.
- (17) Han, C.-H.; Han, S.-D.; Gwak, J.; Khatkar, S. Synthesis of indium tin oxide (ITO) and fluorine-doped tin oxide (FTO) nanopowder by sol-gel combustion hybrid method. *Mater. Lett.* **2007**, *61*, 1701–1703.
- (18) Terrier, C.; Chatelon, J.; Roger, J. Electrical and optical properties of Sb:SnO<sub>2</sub> thin films obtained by the sol-gel method. *Thin Solid Films* **1997**, *295*, 95–100.
- (19) Bissig, B.; Jäger, T.; Ding, L.; Tiwari, A. N.; Romanyuk, Y. E. Limits of carrier mobility in Sb-doped SnO<sub>2</sub> conducting films deposited by reactive sputtering. *APL Mater.* **2015**, *3*, 062802.
- (20) Swallow, J. E. N.; Williamson, B. A. D.; Whittles, T. J.; Birkett, M.; Featherstone, T. J.; Peng, N.; Abbott, A.; Farnworth, M.; Cheetham, K. J.; Warren, P.; Scanlon, D. O.; Dhanak, V. R.; Veal, T. D. Self-Compensation in Transparent Conducting F-Doped SnO<sub>2</sub>. *Adv. Funct. Mater.* **2018**, *28*, 1701900.
- (21) White, M. E.; Bierwagen, O.; Tsai, M. Y.; Speck, J. S. Electron transport properties of antimony doped SnO<sub>2</sub> single crystalline thin

films grown by plasma-assisted molecular beam epitaxy. *J. Appl. Phys.* **2009**, *106*, 093704.

(22) Berry, F. J.; Laundry, B. J. Note. Antimony-121 Mössbauer study of the effects of calcination on the structure of tin–antimony oxides. *J. Chem. Soc., Dalton Trans.* **1981**, 1442–1444.

(23) Gržeta, B.; Tkalčec, E.; Goebbert, C.; Takeda, M.; Takahashi, M.; Nomura, K.; Jakšić, M. Structural studies of nanocrystalline SnO<sub>2</sub> doped with antimony: XRD and Mössbauer spectroscopy. *J. Phys. Chem. Solids* **2002**, *63*, 765–772.

(24) Terrier, C.; Chatelon, J.; Roger, J.; Berjoan, R.; Dubois, C. Analysis of Antimony Doping in Tin Oxide Thin Films Obtained by the Sol-Gel Method. *J. Sol-Gel Sci. Technol.* **1997**, *10*, 75–81.

(25) Montilla, F.; Morallon, E.; De Battisti, A.; Barison, S.; Daolio, S.; Vazquez, J. L. Preparation and Characterization of Antimony-Doped Tin Dioxide Electrodes. 3. XPS and SIMS Characterization. *J. Phys. Chem. B* **2004**, *108*, 15976–15981.

(26) Geraldo, V.; Briois, V.; Scalvi, L.; Santilli, C. EXAFS investigation on Sb incorporation effects to electrical transport in SnO<sub>2</sub> thin films deposited by sol–gel. *J. Eur. Ceram. Soc.* **2007**, *27*, 4265–4268.

(27) Rockenberger, J.; zum Felde, U.; Tischer, M.; Tröger, L.; Haase, M.; Weller, H. Near edge X-ray absorption fine structure measurements (XANES) and extended x-ray absorption fine structure measurements (EXAFS) of the valence state and coordination of antimony in doped nanocrystalline SnO<sub>2</sub>. *J. Chem. Phys.* **2000**, *112*, 4296–4304.

(28) Bhachu, D. S.; Scanlon, D. O.; Sankar, G.; Veal, T. D.; Egdell, R. G.; Cibir, G.; Dent, A. J.; Knapp, C. E.; Carmalt, C. J.; Parkin, I. P. Origin of High Mobility in Molybdenum-Doped Indium Oxide. *Chem. Mater.* **2015**, *27*, 2788–2796.

(29) Swallow, J. E. N.; et al. Resonant Doping for High Mobility Transparent Conductors: the Case of Mo-doped In<sub>2</sub>O<sub>3</sub>. *Mater. Horiz.* **2020**, *7*, 236–243.

(30) Walsh, A.; Sokol, A. A.; Buckeridge, J.; Scanlon, D. O.; Catlow, C. R. A. Oxidation states and ionicity. *Nat. Mater.* **2018**, *17*, 958–964.

(31) Abe, Y.; Ishiyama, N. Titanium-doped indium oxide films prepared by d.c. magnetron sputtering using ceramic target. *J. Mater. Sci.* **2006**, *41*, 7580–7584.

(32) Morales-Masis, M.; Rucavado, E.; Monnard, R.; Barraud, L.; Holovsky, J.; Despeisse, M.; Boccard, M.; Ballif, C. Highly conductive and broadband transparent Zr-doped In<sub>2</sub>O<sub>3</sub> as front electrode for solar cell. *IEEE journal of photovoltaics* **2018**, *8*, 1202–1207.

(33) Wang, G.; Shi, C.; Zhao, L.; Diao, H.; Wang, W. Transparent conductive Hf-doped In<sub>2</sub>O<sub>3</sub> thin films by RF sputtering technique at low temperature annealing. *Appl. Surf. Sci.* **2017**, *399*, 716–720.

(34) Abe, Y.; Ishiyama, N. Polycrystalline films of tungsten-doped indium oxide prepared by d.c. magnetron sputtering. *Mater. Lett.* **2007**, *61*, 566–569.

(35) Egdell, R. G.; Gulino, A.; Rayden, C.; Peacock, G.; Cox, P. A. Nature of donor states in V-doped SnO<sub>2</sub>. *J. Mater. Chem.* **1995**, *5*, 499–504.

(36) Suzuki, A. Y.; Nose, K.; Ueno, A.; Kamiko, M.; Mitsuda, Y. High Transparency and Electrical Conductivity of SnO<sub>2</sub>:Nb Thin Films Formed through (001)-Oriented SnO:Nb on Glass Substrate. *Appl. Phys. Express* **2012**, *5*, 011103.

(37) Gokulakrishnan, V.; Parthiban, S.; Jeganathan, K.; Ramamurthi, K. Investigations on the structural, optical and electrical properties of Nb-doped SnO<sub>2</sub> thin films. *J. Mater. Sci.* **2011**, *46*, 5553–5558.

(38) Seo, Y. J.; Kim, G. W.; Sung, C. H.; Anwar, M.; Lee, C. G.; Koo, B. H. Characterization of transparent and conductive electrodes of Nb-doped SnO<sub>2</sub> thin film by pulsed laser deposition. *Curr. Appl. Phys.* **2011**, *11*, S310–S313.

(39) Nakao, S.; Yamada, N.; Hitosugi, T.; Hirose, Y.; Shimada, T.; Hasegawa, T. High Mobility Exceeding 80 cm<sup>2</sup> V<sup>-1</sup> s<sup>-1</sup> in Polycrystalline Ta-Doped SnO<sub>2</sub> Thin Films on Glass Using Anatase TiO<sub>2</sub> Seed Layers. *Appl. Phys. Express* **2010**, *3*, 031102.

(40) Lee, S. W.; Kim, Y.-W.; Chen, H. Electrical properties of Ta-doped SnO<sub>2</sub> thin films prepared by the metal–organic chemical-vapor deposition method. *Appl. Phys. Lett.* **2001**, *78*, 350–352.

(41) Kim, Y.-W.; Lee, S. W.; Chen, H. Microstructural evolution and electrical property of Ta-doped SnO<sub>2</sub> films grown on Al<sub>2</sub>O<sub>3</sub> (0001) by metalorganic chemical vapor deposition. *Thin Solid Films* **2002**, *405*, 256–262.

(42) Lee, S.; Daga, A.; Xu, Z.; Chen, H. Characterization of MOCVD grown optical coatings of Sc<sub>2</sub>O<sub>3</sub> and Ta-doped SnO<sub>2</sub>. *Mater. Sci. Eng., B* **2003**, *99*, 134–137.

(43) Nakao, S.; Yamada, N.; Hitosugi, T.; Hirose, Y.; Shimada, T.; Hasegawa, T. Fabrication of highly conductive Ta-doped SnO<sub>2</sub> polycrystalline films on glass using seed-layer technique by pulse laser deposition. *Thin Solid Films* **2010**, *518*, 3093–3096.

(44) Toyosaki, H.; Kawasaki, M.; Tokura, Y. Electrical properties of Ta-doped SnO<sub>2</sub> thin films epitaxially grown on TiO<sub>2</sub> substrate. *Appl. Phys. Lett.* **2008**, *93*, 132109.

(45) Turgut, G. Effect of Ta doping on the characteristic features of spray-coated SnO<sub>2</sub>. *Thin Solid Films* **2015**, *594*, 56–66.

(46) Muto, Y.; Nakatomi, S.; Oka, N.; Iwabuchi, Y.; Kotsubo, H.; Shigesato, Y. High-rate deposition of Ta-doped SnO<sub>2</sub> films by reactive magnetron sputtering using a Sn–Ta metal-sintered target. *Thin Solid Films* **2012**, *520*, 3746–3750.

(47) Nguyen, N. M.; Luu, M. Q.; Nguyen, M. H.; Nguyen, D. T.; Bui, V. D.; Truong, T. T.; Pham, V. T.; Nguyen-Tran, T. Synthesis of Tantalum-Doped Tin Oxide Thin Films by Magnetron Sputtering for Photovoltaic Applications. *J. Electron. Mater.* **2017**, *46*, 3667–3673.

(48) Weidner, M.; Jia, J.; Shigesato, Y.; Klein, A. Comparative study of sputter-deposited SnO<sub>2</sub> films doped with antimony or tantalum. *Phys. Status Solidi B* **2016**, *253*, 923–928.

(49) Weidner, M.; Brötz, J.; Klein, A. Sputter-deposited polycrystalline tantalum-doped SnO<sub>2</sub> layers. *Thin Solid Films* **2014**, *555*, 173–178.

(50) Yamada, N.; Nakao, S.; Hitosugi, T.; Hasegawa, T. Sputter Deposition of High-Mobility Sn<sub>1-x</sub>Ta<sub>x</sub>O<sub>2</sub> Films on Anatase-TiO<sub>2</sub>-Coated Glass. *Jpn. J. Appl. Phys.* **2010**, *49*, 108002.

(51) Kresse, G.; Hafner, J. *Ab-initio* molecular-dynamics simulation of the liquid-metal-amorphous-semiconductor transition in germanium. *Phys. Rev. B: Condens. Matter Mater. Phys.* **1994**, *49*, 14251–14269.

(52) Kresse, G.; Hafner, J. *Ab-initio* molecular dynamics for liquid metals. *Phys. Rev. B: Condens. Matter Mater. Phys.* **1993**, *47*, 558–561.

(53) Kresse, G.; Furthmüller, J. Efficiency of *ab-initio* total energy calculations for metals and semiconductors using a plane-wave basis set. *Comput. Mater. Sci.* **1996**, *6*, 15–50.

(54) Kresse, G.; Furthmüller, J. Efficient iterative schemes for *ab-initio* total-energy calculations using a plane-wave basis set. *Phys. Rev. B: Condens. Matter Mater. Phys.* **1996**, *54*, 11169–11186.

(55) Blöchl, P. E. Projector augmented-wave method. *Phys. Rev. B: Condens. Matter Mater. Phys.* **1994**, *50*, 17953–17979.

(56) Kresse, G.; Joubert, D. From ultrasoft pseudopotentials to the projector augmented-wave method. *Phys. Rev. B: Condens. Matter Mater. Phys.* **1999**, *59*, 1758–1775.

(57) Adamo, C.; Barone, V. Toward reliable density functional methods without adjustable parameters: The PBE0 model. *J. Chem. Phys.* **1999**, *110*, 6158–6170.

(58) Paier, J.; Hirschl, R.; Marsman, M.; Kresse, G. The Perdew–Burke–Ernzerhof exchange–correlation functional applied to the G2–1 test set using a plane-wave basis set. *J. Chem. Phys.* **2005**, *122*, 234102.

(59) Perdew, J. P.; Burke, K.; Ernzerhof, M. Generalized Gradient Approximation made simple. *Phys. Rev. Lett.* **1996**, *77*, 3865–3868.

(60) Scanlon, D. O.; Watson, G. W. On the possibility of p-type SnO<sub>2</sub>. *J. Mater. Chem.* **2012**, *22*, 25236–25245.

(61) Ganose, A. M.; Scanlon, D. O. Band gap and work function tailoring of SnO<sub>2</sub> for improved transparent conducting ability in photovoltaics. *J. Mater. Chem. C* **2016**, *4*, 1467–1475.

(62) Vasheghani Farahani, S. K.; Veal, T. D.; Mudd, J. J.; Scanlon, D. O.; Watson, G. W.; Bierwagen, O.; White, M. E.; Speck, J. S.; McConville, C. F. Valence-band density of states and surface electron accumulation in epitaxial SnO<sub>2</sub> films. *Phys. Rev. B: Condens. Matter Mater. Phys.* **2014**, *90*, 155413.

- (63) Lebens-Higgins, Z.; Scanlon, D.; Paik, H.; Sallis, S.; Nie, Y.; Uchida, M.; Quackenbush, N.; Wahila, M.; Sterbinsky, G.; Arena, D. A.; Woicik, J.; Schlom, D.; Piper, L. Direct Observation of Electrostatically Driven Band Gap Renormalization in a Degenerate Perovskite Transparent Conducting Oxide. *Phys. Rev. Lett.* **2016**, *116*, 027602.
- (64) Sallis, S.; Scanlon, D. O.; Chae, S. C.; Quackenbush, N. F.; Fischer, D. A.; Woicik, J. C.; Guo, J.-H.; Cheong, S. W.; Piper, L. F. J. La-doped SnO<sub>2</sub> - Degenerate perovskite transparent conducting oxide: Evidence from synchrotron x-ray spectroscopy. *Appl. Phys. Lett.* **2013**, *103*, 042105.
- (65) Scanlon, D. O. Defect engineering of BaSnO<sub>3</sub> for high-performance transparent conducting oxide applications. *Phys. Rev. B: Condens. Matter Mater. Phys.* **2013**, *87*, 161201.
- (66) Agoston, P.; Körber, C.; Klein, A.; Puska, M. J.; Nieminen, R. M.; Albe, K. Limits for n-type doping in In<sub>2</sub>O<sub>3</sub> and SnO<sub>2</sub>: A theoretical approach by first-principles calculations using hybrid-functional methodology. *J. Appl. Phys.* **2010**, *108*, 053511.
- (67) Agoston, P.; Albe, K.; Nieminen, R. M.; Puska, M. J. Intrinsic n-Type Behavior in Transparent Conducting Oxides: A Comparative Hybrid-Functional Study In<sub>2</sub>O<sub>3</sub>, SnO<sub>2</sub> and ZnO. *Phys. Rev. Lett.* **2009**, *103*, 245501.
- (68) Grauzinytė, M.; Goedecker, S.; Flores-Livas, J. A. Computational Screening of Useful Hole–Electron Dopants in SnO<sub>2</sub>. *Chem. Mater.* **2017**, *29*, 10095–10103.
- (69) Powell, M. J.; Williamson, B. A. D.; Baek, S.-Y.; Manzi, J.; Potter, D. B.; Scanlon, D. O.; Carmalt, C. J. Phosphorus doped SnO<sub>2</sub> thin films for transparent conducting oxide applications: synthesis, optoelectronic properties and computational models. *Chemical Science* **2018**, *9*, 7968–7980.
- (70) Van de Walle, C. G.; Neugebauer, J. First-principles calculations for defects and impurities: Applications to III-nitrides. *J. Appl. Phys.* **2004**, *95*, 3851–3879.
- (71) Lany, S.; Zunger, A. Assessment of correction methods for the band-gap problem and for finite-size effects in supercell defect calculations: Case studies for ZnO and GaAs. *Phys. Rev. B: Condens. Matter Mater. Phys.* **2008**, *78*, 235104.
- (72) Hine, N. D. M.; Frensch, K.; Foulkes, W. M. C.; Finnis, M. W. Supercell size scaling of density functional theory formation energies of charged defects. *Phys. Rev. B: Condens. Matter Mater. Phys.* **2009**, *79*, 024112.
- (73) Reuter, K.; Scheffler, M. Composition, structure, and stability RuO<sub>2</sub> (110) as a function of oxygen pressure. *Phys. Rev. B: Condens. Matter Mater. Phys.* **2001**, *65*, 035406.
- (74) Medeiros, P. V. C.; Stafström, S.; Björk, J. Effects of extrinsic and intrinsic perturbations on the electronic structure of graphene: Retaining an effective primitive cell band structure by band unfolding. *Phys. Rev. B: Condens. Matter Mater. Phys.* **2014**, *89*, 041407.
- (75) Medeiros, P. V. C.; Tsirkin, S. S.; Stafström, S.; Björk, J. Unfolding spinor wave functions and expectation values of general operators: Introducing the unfolding-density operator. *Phys. Rev. B: Condens. Matter Mater. Phys.* **2015**, *91*, 041116.
- (76) Williamson, B. A. D.; Buckeridge, J.; Chadwick, N. P.; Sathasivam, S.; Carmalt, C. J.; Parkin, I. P.; Scanlon, D. O. Dispelling the Myth of Passivated Codoping in TiO<sub>2</sub>. *Chem. Mater.* **2019**, *31*, 2577–2589.
- (77) Button, K. J.; Fonstad, C. G.; Dreybrodt, W. Determination of the Electron Masses in Stannic Oxide by Submillimeter Cyclotron Resonance. *Phys. Rev. B* **1971**, *4*, 4539–4542.
- (78) Thangaraju, B. Structural and electrical studies on highly conducting spray deposited fluorine and antimony doped SnO<sub>2</sub> thin films from SnCl<sub>2</sub> precursor. *Thin Solid Films* **2002**, *402*, 71–78.
- (79) Jäger, S.; Szyszka, B.; Szczyrbowski, J.; Bräuer, G. Comparison of transparent conductive oxide thin films prepared by a.c. and d.c. reactive magnetron sputtering. *Surf. Coat. Technol.* **1998**, *98*, 1304–1314.
- (80) Turgut, G.; Keskenler, E. F.; Aydın, S.; Sönmez, E.; Doğan, S.; Düzgün, B.; Ertuğrul, M. Effect of Nb doping on structural, electrical and optical properties of spray deposited SnO<sub>2</sub> thin films. *Superlattices Microstruct.* **2013**, *56*, 107–116.
- (81) Aydın, E.; De Bastiani, M.; Yang, X.; Sajjad, M.; Aljamaan, F.; Smirnov, Y.; Hedhili, M. N.; Liu, W.; Allen, T. G.; Xu, L.; Van Kerschaver, E.; Morales-Masis, M.; Schwingenschlogl, U.; De Wolf, S. Zr-Doped Indium Oxide (IZRO) Transparent Electrodes for Perovskite-Based Tandem Solar Cells. *Adv. Funct. Mater.* **2019**, *29*, 1901741.
- (82) Nag, B. R. *Electron Transport in Compound Semiconductors*; Springer-Verlag, 1980; p 29.
- (83) Rey, G.; Ternon, C.; Modreanu, M.; Mescot, X.; Consonni, V.; Bellet, D. Electron scattering mechanisms in fluorine-doped SnO<sub>2</sub> thin films. *J. Appl. Phys.* **2013**, *114*, 183713.
- (84) Pelliccione, C. J.; Timofeeva, E. V.; Segre, C. U. Potential-Resolved In Situ X-ray Absorption Spectroscopy Study of Sn and SnO<sub>2</sub> Nanomaterial Anodes for Lithium-Ion Batteries. *J. Phys. Chem. C* **2016**, *120*, 5331–5339.